photonics

MDPI

Article

Grooved High-Reflective Films for Ultraviolet Emission Enhancement

Hengrui Zhang, Zhanhua Huang and Lin Zhang *

State Key Laboratory of Precision Measuring Technology and Instruments, Key Laboratory of Opto-Electronic Information Technology of Ministry of Education, Tianjin Key Laboratory of Integrated Opto-Electronics Technologies and Devices, School of Precision Instruments and Opto-Electronics Engineering, Tianjin University, Tianjin 300072, China; hengruizhang@tju.edu.cn (H.Z.); zhanhua@tju.edu.cn (Z.H.)
* Correspondence: lin_zhang@tju.edu.cn

Abstract

Conventional ultraviolet microplasma sources typically lack a back-reflection structure, resulting in radiative power loss from the backside. To enhance the emission efficiency of ultraviolet microplasma devices around 220 nm, we propose a multilayer reflective coating composed of alternating high- and low-refractive-index layers of Al_2O_3 and SiO_2, within a V-shaped groove. Key structural parameters, including the number of alternating film layer pairs, groove width, and light source position, are investigated to show their effects on ultraviolet reflection characteristics. The results show that reducing the groove width greatly enhances light reflection. When the groove width is 6.5 μm, the device exhibits a reflection efficiency of 47.82% and power enhancement of 91.66%, representing improvements of 2.5-fold and 4.2-fold, respectively, compared to non-optimized cases. Device performance is also influenced by the offset of the light source, which is more sensitive along the horizontal direction. This study provides a practical solution for developing high-efficiency ultraviolet emission devices.

Keywords: ultraviolet high-reflective films; groove-shaped device; emission enhancement

Received: 16 May 2025
Revised: 18 June 2025
Accepted: 24 June 2025
Published: 25 June 2025

Citation: Zhang, H.; Huang, Z.; Zhang, L. Grooved High-Reflective Films for Ultraviolet Emission Enhancement. *Photonics* **2025**, *12*, 644. https://doi.org/10.3390/photonics12070644

1. Introduction

Microplasma, a novel form of electrical discharge, have attracted considerable attention due to their high energy density, elevated plasma density, and exceptional spatiotemporal stability at the microscale [1–3]. Compared to conventional plasmas, microplasma can be generated and sustained at or below atmospheric pressure with appropriate design, enabling the formation of micrometer-scale discharges while significantly reducing system complexity and cost. Microplasma has been extensively studied and applied across various fields, including ultraviolet (UV) light sources [4–7], beam steering [8,9], microchemical analysis systems [10], biomedicine [11,12], and material surface modification [13], due to their excellent controllability and broad applications. Ultraviolet light sources operate within a frequency range of 7.5×10^{14} Hz to 3×10^{16} Hz, corresponding to vacuum wavelengths of 10–400 nm. Ultraviolet radiation is classified into four distinct spectral bands based on wavelength range and biological effects: UV-A (315–400 nm), UV-B (280–315 nm), UV-C (100–280 nm), and vacuum ultraviolet (10–100 nm) [14]. Conventional UV-C sources primarily employ mercury vapor lamps that emit light at a wavelength of 254 nm. Preliminary studies suggest that ultraviolet light at 222 nm is equally effective in inactivating viruses and bacteria while offering improved safety for human exposure [15,16].

In recent years, microplasma arrays fabricated using microfabrication techniques have developed rapidly [17–24], in which the spatial confinement and coordinated control of plasma, enabled by the periodic arrangement of micron-scale discharge units, are needed. For example, in 1997, Eden's research group at the University of Illinois, USA, fabricated a single-cavity plasma device with a cylindrical structure on a silicon-based substrate using ultrasonic machining [17]. The device had a diameter of 200–400 μm and a depth of 0.5–5 mm. When filled with a gas mixture of 50 Torr Xe and 1 Torr I_2, and operated at an input power of 500 mW, it produced an output power of 270 mW, measured at a distance of 1.4 cm from the device. In 2005, they proposed an inverted-pyramidal microcavity plasma discharge device composed of a 200 × 200 array, with each microcavity in a size of 50 × 50 μm^2 [19]. When driven by a 20 kHz sinusoidal voltage, the device exhibited a luminous efficacy of 7.2 ± 0.6 lm/W and a brightness of 525 ± 75 cd/m^2. In 2017, they engineered a microplasma array consisting of at least two interleaved microcavities [23]. The configuration, which employed two fused silica plates as front and rear windows, produced a planar lamp in the size of 10 × 10 cm^2, with an effective area of 80 cm^2 and a thickness of less than 6 mm. The device is operated in a 54% Xe/Ne gas mixture at 550 Torr, with an electro-optical conversion efficiency exceeding 20%. However, due to the absence of a back-reflection structure, over 40% of the radiated power is lost through the backside. This emphasizes the importance of adding reflective multilayers. In 2020, Dzikowski et al. from Ruhr University Bochum, Germany, introduced a modular metallic grating microcavity plasmonic array [24]. The array consisted of several hundred uniformly distributed apertures, each with a diameter of 150 μm, and employed magnetic forces to maintain the structural integrity of the assembly. Current research on ultraviolet light source devices primarily focuses on the design of microcavity array architectures and the enhancement of emission intensity. In contrast, systematic studies aimed at efficient UV light collection, output amplification, and improved energy utilization remain relatively limited. Consequently, effectively enhancing the output of ultraviolet light at specific wavelengths is essential for improving the overall performance of plasma emission systems.

The high resolution and repeatability of advanced lithography and etching techniques in micro–nano fabrication processes provide a solid foundation for the integration and miniaturization of multifunctional devices. Reflective thin films for ultraviolet applications can be highly effective via multilayer interference. In 2014, Sun et al. at the Shanghai Institute of Optics and Fine Mechanics designed an Al_2O_3/AlF_3 reflective coating [25]. A reflectance of 98.1% was achieved in the 180–200 nm spectral range. In 2017, Narukage et al. from the National Astronomical Observatory of Japan designed a MgF_2/LaF_3 reflective filter [26], achieving a peak reflectance of 57% at 121.6 nm. However, the stability of these reflective coatings is compromised by the degradation and contamination of fluoride materials during storage. Although a ZrO_2/Al_2O_3 bandpass filter was reported in 2023 for suppressing long-wavelength emissions in the 240–270 nm range from KrCl* excimer lamps operating at 222 nm [27], it is even more noteworthy that recent advances since 2020 in fields, such as metasurface reflectors, temporal modulation, and 3D photonic crystals, would inspire great progresses in device innovations [28–30].

In this paper, we study a groove-shaped ultraviolet high-reflective film based on COMS-compatible fabrication, to enhance the luminous efficiency and upward output of UV microplasma devices. Structural design and optimization are conducted. On one hand, the groove width plays a crucial role in determining the reflective performance of the groove-shaped device. When the groove width is set to 6.5 μm, the device achieves optimal reflective performance, with a reflectance efficiency of up to 47.82% and a power enhancement of 91.66%, representing 2.5-fold and 4.2-fold improvements, respectively, compared to the non-optimized case. On the other hand, displacement of the light source has a

pronounced effect on device's performance. Horizontal displacement causes substantial performance variations, while vertical displacement exhibits spatial selectivity.

2. Structural Design

We propose a groove-shaped device to build a microcavity for microplasma, while a high-reflectivity multilayer coating is used to enhance the upward light extraction efficiency of ultraviolet emission systems, with its cross-sectional view shown in Figure 1a. Here, W denotes the groove opening width, and the apex angle is 68°, which is determined by wet etching of silicon. We design the multilayer reflective films composed of alternating layers of Al_2O_3 and SiO_2, centered at a wavelength of 220 nm. Al_2O_3 serves as the high-refractive-index material, while SiO_2 functions as the low-refractive-index material. Silicon wafers are selected as the substrate, onto which Al_2O_3 and SiO_2 can be alternately formed using the atomic layer deposition process. The final structure includes a terminating layer of Al_2O_3 and can be represented as $Si/(HL)^mH/Air$, where H denotes Al_2O_3, L denotes SiO_2, m is the number of alternating periods, and the total number of layers is $2m + 1$. The optical thickness of each film layer is set to $\lambda/4n$, where λ is the designed central wavelength in vacuum, and n is the refractive index of the corresponding film material. Based on the effective interface method [31] for multilayer films, the reflectance of the structure under normal incidence and at the central wavelength can be obtained through a layer-by-layer calculation as follows:

$$\rho_\lambda = \left[\frac{n_0 - \left(\frac{n_H}{n_L}\right)^{2m} \frac{n_H^2}{n_G}}{n_0 + \left(\frac{n_H}{n_L}\right)^{2m} \frac{n_H^2}{n_G}} \right]^2, \quad (1)$$

where n_0 is the refractive index of the incident medium, typically assumed to be 1, while n_H and n_L are the refractive indices of the high- and low-index layers, respectively. A larger contrast between n_H and n_L, along with an increased total number of layers, results in higher reflectance of the multilayer film structure. According to the experimental report [32,33], the refractive indices of Al_2O_3 and SiO_2 at 220 nm are set to n_H = 1.7975 and n_L = 1.5355, respectively.

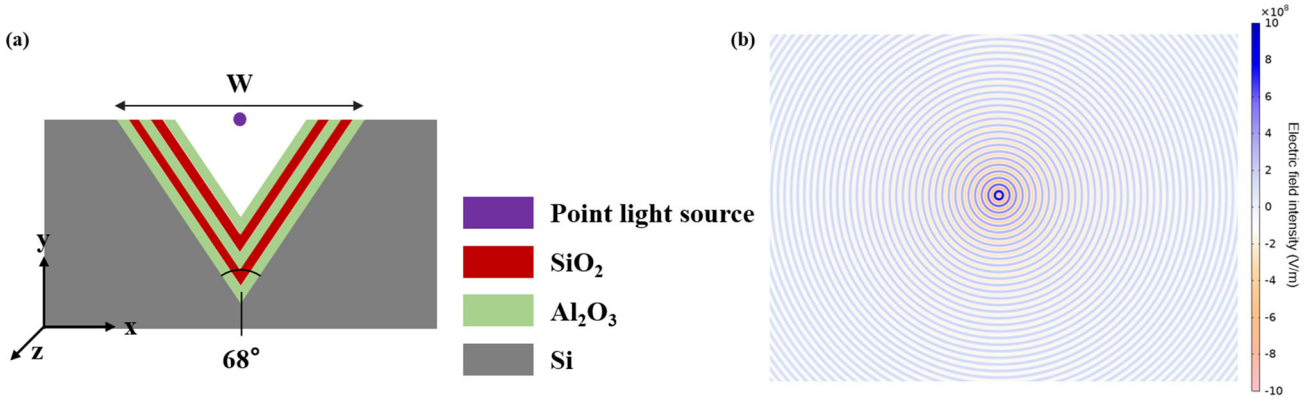

Figure 1. (**a**) Schematic cross-sectional view of the groove-shaped device. (**b**) Simulated electric field intensity distribution from a point source within the device.

To quantitatively evaluate the reflective performance, we investigate two cases: one without the coatings and another with the reflective coatings. By comparing the electric field distributions and far-field radiation patterns between these two cases, the improvement in ultraviolet light reflection provided by the groove-shaped film can be clearly observed.

The light source excited by the microplasma has its radiation characteristics approximated as those of an ideal point source. The electric field distribution shown in Figure 1b is obtained by simulating the radiation of a point source using finite-element modeling.

Specifically, the point source is approximated using the line current setting. The field distribution of the point source exhibits a standard spherical wavefront, consistent with the propagation behavior of a point source in an ideal homogeneous medium.

3. Results and Discussion

3.1. Analysis of the Influence of Alternating Film Layer Periods

We calculated the reflection spectra under normal incidence over the wavelength range of 180 to 260 nm for four different multilayer structures with alternating period numbers of m = 5, 7, 9, and 11, using the Transfer Matrix Method. As shown in Figure 2, the reflectance of the films increases significantly with the number of alternating periods.

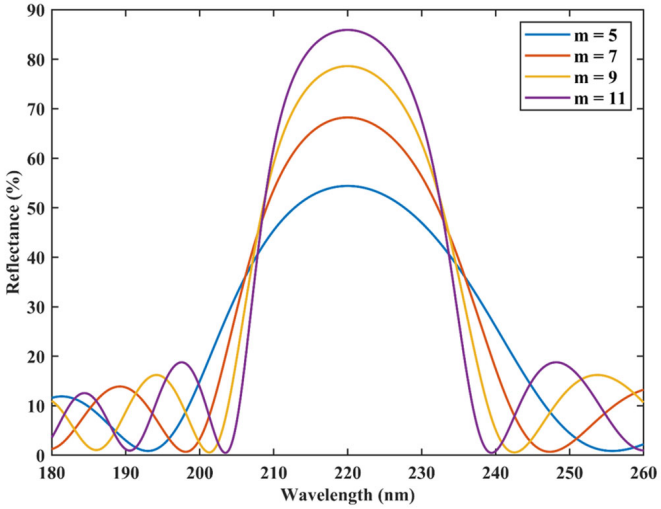

Figure 2. Reflection spectra for different numbers of alternating film layer periods.

Specifically, when m = 5, the reflection peak is relatively broad and smooth, with a reflectance of 54.41%. When m = 7, a secondary peak begins to emerge on the shorter-wavelength side, and the reflectance increases to 68.24%. As m increases further, the secondary peak structure becomes more pronounced, exhibiting multiple distinct periodic sub-peaks. When m = 11, the reflectance reaches 85.93%, with a full width at half maximum of 25.45 nm.

In addition to normal incidence, oblique incidence should also be considered. Figure 3 shows the variation in reflectance at different incident angles for m = 11. At an incident angle of 10°, the reflection spectrum exhibits only a slight shift compared to normal incidence. The central wavelength of the main peak remains close to 220 nm, with a slight shift toward the shorter wavelength region. As the incident angle increases to 30°, the main peak shifts further toward shorter wavelengths, and the peak reflectance exhibits a slight decreasing trend. This phenomenon can be attributed to the decrease in the effective optical path length within the multilayer films as the incident angle increases, causing a blue shift of the central wavelength. Additionally, the reflectance coefficients of the polarized components at the interfaces between high- and low-refractive-index materials vary with incident angle, leading to a moderate reduction in overall reflectance. When the incident angle increases to 50°, noticeable changes occur in the spectral profile. The main reflection peak shifts to around 200 nm, while a pronounced minimum appears near 220 nm. At an incident angle of 70°, the reflection spectrum shows further redistribution of peaks and valleys. The main peak shifts toward 190 nm, with the peak reflectance reduced to 70%, and a secondary minimum appears near 220 nm. This indicates that at large incident angles, the phase-matching conditions within the multilayer stack are significantly restructured for different wavelengths. Consequently, the primary high-reflectance band formed under normal or

small-angle incidence may become redistributed into multiple secondary interference peaks, thereby reducing reflectance at the design wavelength. In general, the reflective behavior of the multilayer structure exhibits angular dependence. As the incident angle increases, the reflection peak shifts toward shorter wavelengths, accompanied by a noticeable reduction in peak reflectance.

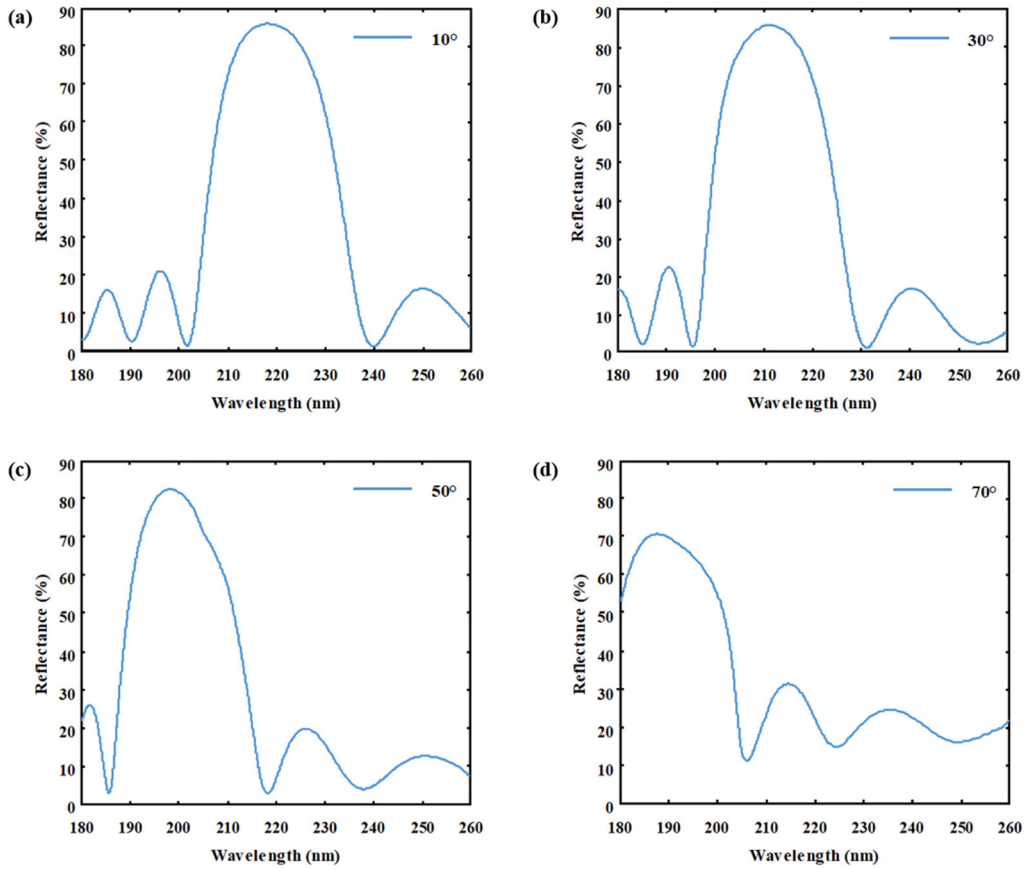

Figure 3. Reflection spectra at different incident angles for m = 11. (**a**) Incident angle of 10°. (**b**) Incident angle of 30°. (**c**) Incident angle of 50°. (**d**) Incident angle of 70°.

In practice, the angle of incidence on the film surface varies depending on the positions of the point light sources. Therefore, considering only normal incidence or a single oblique angle is insufficient to characterize the real optical behavior. It is necessary to evaluate the overall reflective performance of the multilayer system and further investigate its response to radiation from the light source.

3.2. Analysis of the Influence of Groove Width

We use a frequency-domain electromagnetic wave analysis tool, which was built in- house based on the finite element method to obtain the electric field distribution and far-field radiation patterns. We conduct simulations at a wavelength of 220 nm, using the corresponding refractive indices for all materials at 220 nm and applying perfectly matched layers [34] at the boundaries of our computation window. A triangular mesh is applied, with a minimum element size of 15 nm near interfaces and grooves. The near-field electromagnetic response of the device is first computed, and the far-field radiation pattern is then obtained using a far-field transformation. Each V-grooved discharge unit has a depth of about 50 μm [35] perpendicular to the x–y plane as in Figure 1a, which is >200 times the wavelength in vacuum, i.e., 220 nm, making field variation along z-direction negligible. Thus, the electro-magnetic responses of the proposed device in the z-dimension can be

viewed as effectively uniform. To examine the influence of the structural dimensions of the V-shaped groove on reflective performance, we first consider a case with a groove width, W, of 10 μm as an example. The resulting electric field distribution and far-field radiation pattern are shown in Figure 4.

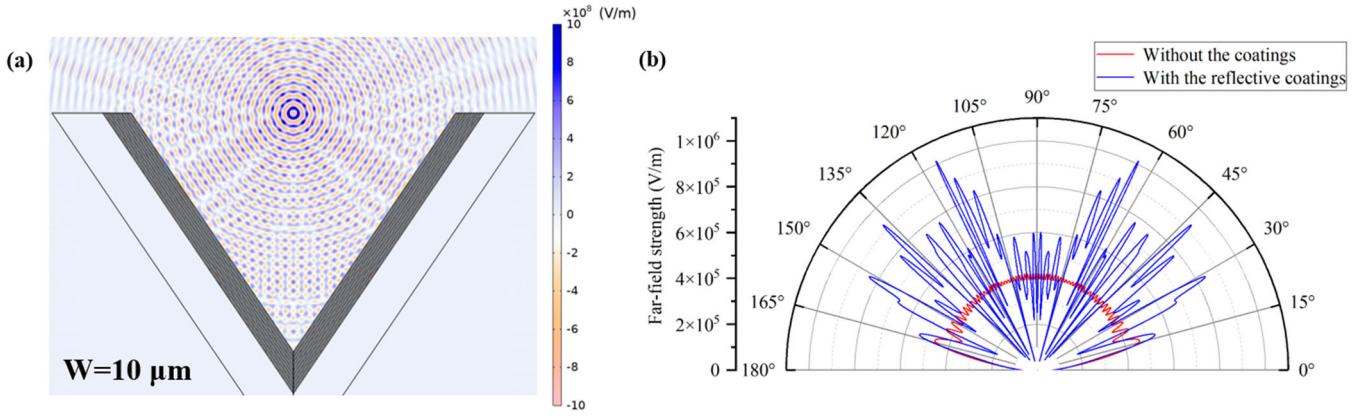

Figure 4. For W = 10 μm, (**a**) electric field intensity distribution and (**b**) far-field radiation pattern are given.

Figure 4a shows the electric field distribution. Compared to Figure 1b, multiple reflections of electromagnetic waves occur within the V-shaped groove, resulting in the formation of complex standing waves and interference fringes, which indicate local field enhancement. Due to the refractive index contrast between the high- and low-index layers of the multilayer structure, the incident electromagnetic wave undergoes successive partial reflections and transmissions at each interface. These processes cause effective interference between the reflected and transmitted waves within the microscale groove, thereby forming a stable standing wave field distribution. Figure 4b shows the far-field radiation pattern. In the case without the coatings, it exhibits a hemispherical distribution with uniformly distributed energy. In contrast, the presence of several sharp lobes in the case with the reflective coatings suggests that multilayer reflections within the groove lead to a complex far-field radiation pattern. Moreover, the magnitude of the far-field mode shows that the lobe intensity in the case with reflective coatings, which spans angular ranges of approximately 60–75° and 105–120°, is nearly twice that of the case without the coatings, further confirming that multiple reflections within the groove cause constructive interference and upward enhancement.

To quantitatively evaluate the reflective performance of the groove, we further introduce reflection efficiency and power enhancement. These are inspired by prior studies that report relative metrics such as luminescence intensity and conversion efficiency [23]. By integrating the far-field radiation patterns corresponding to the case without the coatings and the case with reflective coatings, capturing all upward-emitted components, the associated radiated powers emitted above the groove are obtained and denoted as P_1 and P_2, respectively. These quantities correspond to the output optical power above the device. The reflection efficiency can be defined as follows:

$$\eta = \frac{P_2 - P_1}{P_2}. \tag{2}$$

This ratio represents the proportional contribution of the reflective structure to the far-field radiation and reflects its effective utilization in the total radiated energy. It serves as

a useful metric for evaluating the effectiveness of the proposed device in terms of reducing losses and improving energy utilization. The power enhancement can be defined as follows:

$$G = \frac{P_2 - P_1}{P_1}. \tag{3}$$

This ratio represents the percentage increase in radiation for the case with reflective coatings relative to the case without coatings, indicating the effectiveness of the groove-shaped multilayer device in enhancing overall radiation. It can be used to evaluate the ratio of the increased radiated power to the original radiated power.

The far-field radiation data are integrated, yielding the radiated powers P_1 and P_2 for the cases without and with reflective coatings, respectively. By substituting these values into Equations (1) and (2), the reflection efficiency and power enhancement for W = 10 μm are calculated to be 42.87% and 75.03%, respectively. They are calculated for different groove widths, as shown in Figure 5.

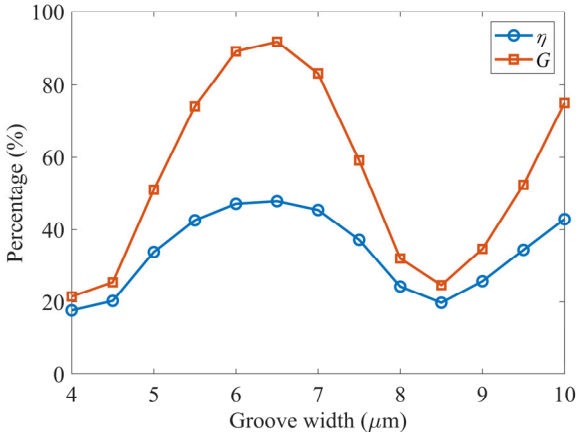

Figure 5. Effects of groove width on reflective performance.

When the groove width is reduced from 10 μm to 8.5 μm, the reflection efficiency decreases to 19.77%, and the power enhancement drops to 24.64%. The corresponding electric field intensity and far-field radiation pattern are shown in Figure 6. As shown in Figure 6a, the multilayer film within the groove continues to change the electric field. However, the interference fringes are significantly less distinct and concentrated compared to the case with W = 10 μm. The electromagnetic waves exhibit increased divergence near the groove opening. Along the reflection path, destructive interference becomes more pronounced, indicating that the optical path differences at multiple positions no longer correspond to integer multiples of the wavelength, thereby suppressing constructive interference. Meanwhile, Figure 6b shows that both the amplitudes and the number of lobes are greatly reduced. The radiation intensity in multiple directions is noticeably weakened, showing that the conditions for multipath interference are no longer satisfied in this case, leading to dispersion and attenuation of the radiated energy.

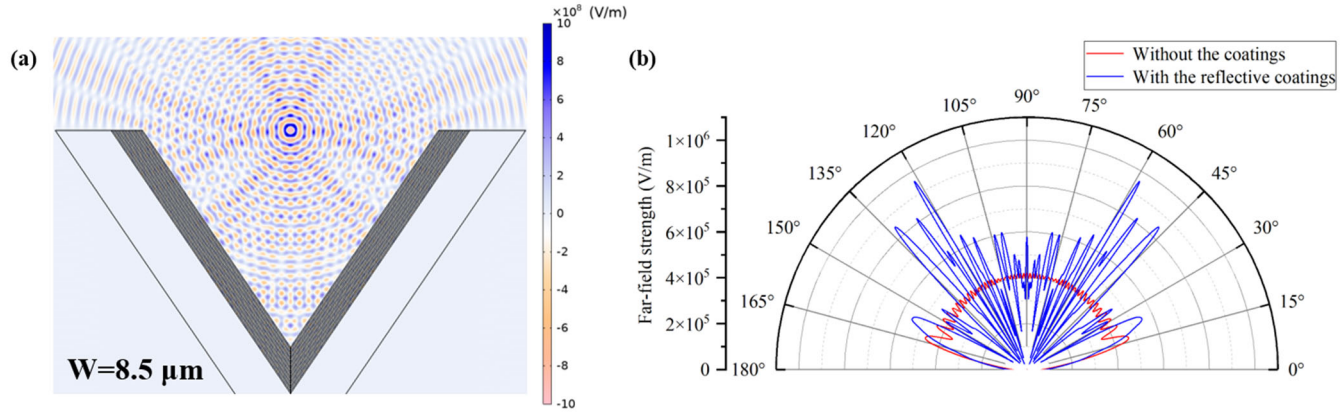

Figure 6. For W = 8.5 μm, (**a**) electric field intensity distribution and (**b**) far-field radiation pattern are given.

When the groove width is further reduced from 8.5 μm to 6.5 μm, the device exhibits optimal reflective performance, with reflection efficiency and power enhancement reaching peak values of approximately 47.82% and 91.66%, respectively. The corresponding electric field intensity and far-field radiation pattern are shown in Figure 7. As shown in Figure 7a, distinct and intense interference fringes are formed within the V-shaped groove, exhibiting strong constructive interference. The electric field is highly concentrated around the groove opening, exhibiting a high-density distribution. The wavefront displays good symmetry and radiates outward in the vertical direction, showing that the energy undergoes multiple reflections within the cavity and is effectively coupled and emitted in a stable direction.

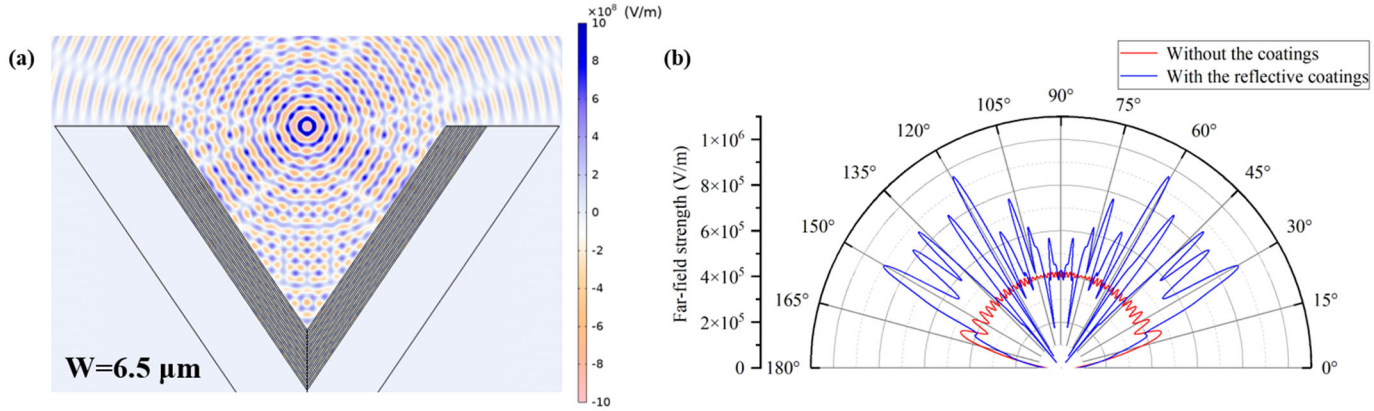

Figure 7. For W = 6.5 μm, (**a**) electric field intensity distribution and (**b**) far-field radiation pattern are given.

As shown in Figure 7b, the number of lobes increases, and the radiation intensity is significantly enhanced in multiple directions compared to Figure 4b. This phenomenon can be attributed to the enhanced phase accumulation effect resulting from multiple reflections within the cavity, which leads to more pronounced interference superposition. As a result, stronger upward radiation characteristics and a more concentrated energy distribution are observed in the far field. Furthermore, the enhancement of lobes also shows that local coherent superposition is simultaneously achieved along multiple interference paths, further improving overall radiation efficiency. Consequently, a groove width of W = 6.5 μm can be considered the optimal design parameter, as it effectively enhances both reflection efficiency and energy output.

As the groove width is further reduced to 4 μm, the reflective performance deteriorates significantly. The reflection efficiency decreases to 17.69%, and the power enhancement

drops to 21.49%. The corresponding electric field intensity distribution is shown in Figure 8. The interference fringes in the V-shaped groove region appear sparse, with an overall reduction in field strength. Although some reflection still occurs within the groove, the reflected wavefronts fail to achieve phase matching, preventing significant coherent superposition. As a result, the energy reutilization efficiency within the structure is substantially reduced. This result indicates that when the groove becomes too narrow, the propagation and reflection paths of the light waves are severely constrained, ultimately leading to a substantial reduction in the structure's ability to release reflected energy. This manifests as a degradation in reflective performance.

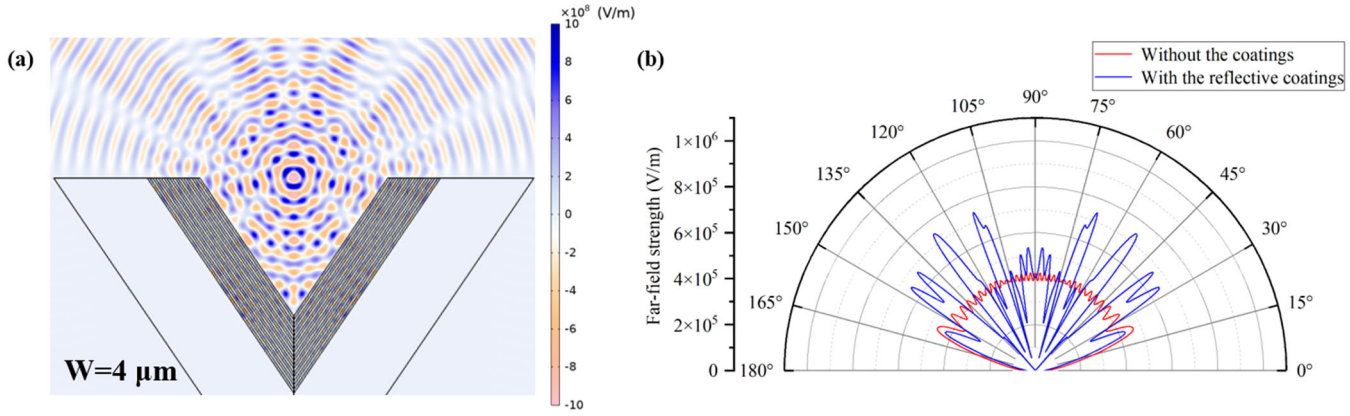

Figure 8. For W = 4 μm, (**a**) electric field intensity distribution and (**b**) far-field radiation pattern are given.

As shown in Figure 8b, although the intensity is slightly enhanced compared to the case without the coatings, the overall radiation remains weak. The far-field energy distribution exhibits a low-intensity diffusion pattern. This radiation pattern shows that under these conditions, the reflected energy within the groove cavity cannot be effectively directed outward. These characteristics indicate that when the groove width is reduced below a certain threshold, the device can no longer establish an effective upward cavity-reflection mechanism. Even though multiple reflections may still occur, the lack of constructive interference leads to dispersed energy distribution. Ultimately causing low far-field output, limited reflection efficiency, and minimal power enhancement.

Therefore, by appropriately tuning the geometric dimensions of the groove, the internal reflection paths, phase accumulation mechanisms, and interference effects of electromagnetic waves can be effectively controlled, resulting in a notable enhancement in the device's reflective performance.

3.3. Analysis of the Influence of Light Source Position

Under practical experimental conditions, the ultraviolet light source generated via microplasma is often not precisely aligned with the geometric center of the groove-shaped device due to inherent limitations in alignment accuracy. Therefore, we further investigate the effects of source offset relative to the center of the groove structure. The results obtained with a groove width of W = 10 μm and the light source positioned at the geometric center of the device serve as the reference. Figure 9 shows the electric field intensity and far-field radiation pattern resulting from a 1 μm offset of the light source along the x-axis, with the groove width and other structural parameters at constant.

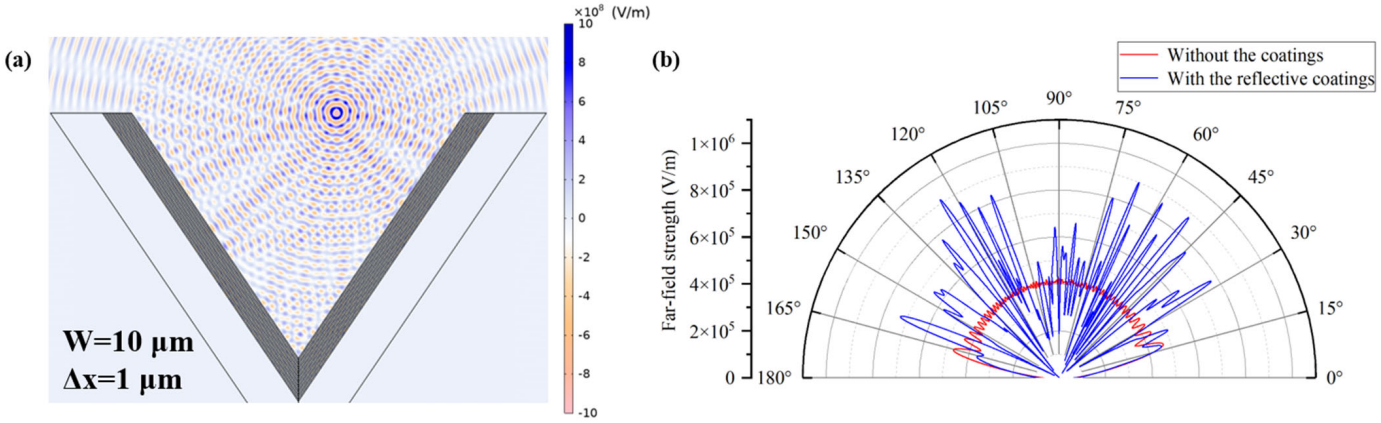

Figure 9. For a 1 μm *x*-axis offset of the light source, (**a**) electric field intensity distribution and (**b**) far-field radiation pattern are given.

When the light source is displaced along the *x*-axis, the wavefronts incident on the left and right walls of the groove experience unequal optical path lengths, leading to an initial phase difference. As shown in Figure 9a, the interference fringes on the right side of the groove become denser with significantly enhanced local field intensity, whereas those on the left side appear sparser with reduced field strength. This asymmetric field enhancement primarily arises from the accumulated phase difference caused by variations in propagation path lengths when the light source is displaced from the central position, resulting in uneven coherent superposition of the reflected waves within the groove.

The corresponding far-field radiation pattern is shown in Figure 9b. It can be observed that the radiation direction no longer exhibits the original symmetrical distribution. The asymmetry in the lobe distribution arises from the optical path difference between the two groove walls. The offset causes shorter optical paths for reflection on the nearer side, resulting in denser and more intense lobes concentrated in 45–75°. Conversely, reflection from the farther side experiences longer paths, leading to sparser lobes distributed between 105 and 135°. This phenomenon shows the complex radiation characteristics resulting from the combined effects of propagation path length differences and interference at the multilayer interfaces under source offset conditions.

The reflection efficiency and power enhancement at different offset values of the light source along the *x*-axis are calculated, as shown in Figure 10.

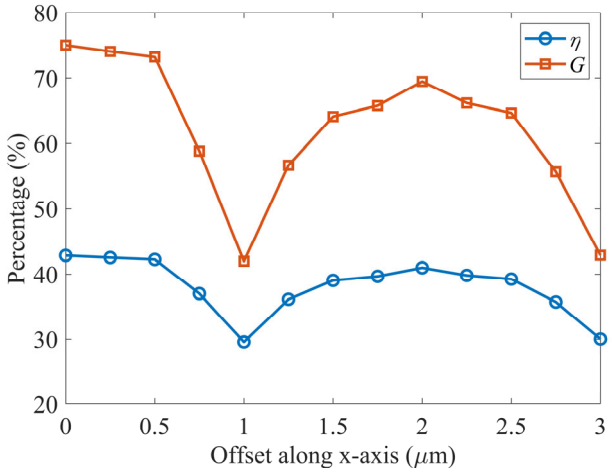

Figure 10. Effects of light source offset along the *x*-axis on reflective performance.

It is observed that as the light source offset increases, the reflection efficiency slightly decreases, reaching a minimum of 29.57% at an offset of 1 μm. Simultaneously, the power enhancement drops significantly to 41.99%, indicating that the structural symmetry is disrupted at this offset, leading to phase interference along the reflected light paths and subsequently reducing the far-field energy output.

When the offset is further increased to 2 μm, both metrics show partial recovery, with the reflection efficiency rising to 40.99% and the power enhancement reaching 69.47%. However, neither returns to the initial values. The corresponding electric field intensity and far-field radiation pattern are shown in Figure 11. The interference fringes of the electric field become increasingly asymmetric, with reflection paths enhanced on the side closer to the offset and weakened on the opposite side. As shown in Figure 11b, the number of lobes increases significantly on the side closer to the offset, accompanied by enhanced radiation intensity in multiple directions. This may be attributed to changes in the incident angle of light at fixed positions on the multilayer surface as the offset increases, causing improved reflective performance compared to the case with a 1 μm offset.

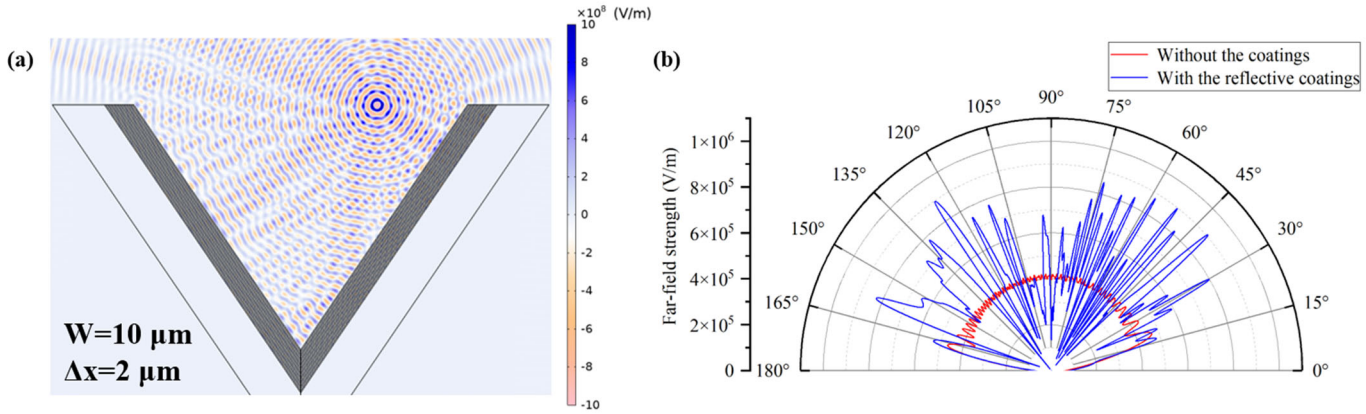

Figure 11. For a 2 μm *x*-axis offset of the light source, (**a**) electric field intensity distribution and (**b**) far-field radiation pattern are given.

However, as the offset continues to increase, the reflective performance drops sharply once again, indicating that the effective reflective region of the structure is spatially bounded. Beyond this range, the radiated energy can no longer be efficiently controlled. This result shows that the groove exhibits high sensitivity to the light source position, and its alignment accuracy directly affects the performance of the reflected radiation.

In addition to the *x*-axis offsets, we also perform simulations and analyses for light source offsets along the *y*-axis. When the light source is offset by 1 μm along the *y*-axis, the electric field intensity and far-field radiation pattern are shown in Figure 12. The light source is positioned closer to the bottom region of the groove, significantly shortening the propagation distance of the initial incident wavefront to the sidewalls and thereby reducing the internal reflection path length of the electromagnetic waves. This change in the propagation path directly causes an overall upward shift of the interference fringes inside the groove, which signifies more energy being funneled toward the groove opening. The regions of enhanced field intensity move noticeably toward the groove opening, and a strong interference-enhanced band appears near the opening region.

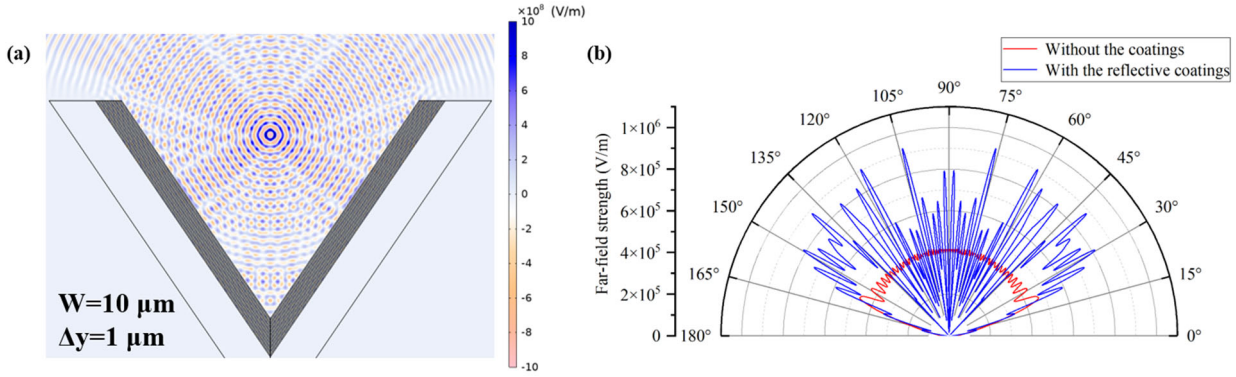

Figure 12. For a 1 μm *y*-axis offset of the light source, (**a**) electric field intensity distribution and (**b**) far-field radiation pattern are given.

Meanwhile, as shown in Figure 12b, when the light source is offset along the *y*-axis, the lobe intensity in the far-field radiation shows no significant change compared to the case where the light source is positioned at the geometric center of the groove. However, it is noteworthy that the number of lobes along the 90° direction increases significantly, accompanied by a denser spacing between lobes. This variation in lobe distribution shows that the downward offset of the light source shortens the initial reflection paths between the groove walls, thereby enhancing the coherent superposition of electromagnetic waves near the groove opening. Consequently, the radiation becomes more strongly concentrated in the direction perpendicular to the groove opening, leading to a more pronounced upward radiation pattern. The reflection efficiency at this offset is calculated to be 42.34%, with a corresponding power enhancement of 73.43%. This result indicates that the device's reflective performance undergoes only a slight reduction and remains within an acceptable range.

Figure 13 shows the variations in reflection efficiency and power enhancement under different *y*-axis offsets of the light source. It is observed that the structure exhibits a periodic response during the y-direction offset process, with performance peaks appearing at multiple offset positions. Specifically, when the offset reaches 0.25 μm, the reflective performance is slightly improved compared to the initial position. As the offset increases to 0.5 μm, both the reflection efficiency and power enhancement drop significantly, reaching 31.6% and 46.2%, respectively. At an offset of 1 μm, both metrics rise again, with the reflection efficiency reaching 45.81% and the power enhancement increasing to 84.55%. As the light source is further offset to 1.5 μm, the performance declines once more. However, at 2 μm, a substantial improvement is observed, with the reflection efficiency and power enhancement reaching 52.96% and 112.59%, respectively, which represent the highest values within the scanned range. Subsequently, a local peak also appears at an offset of 2.75 μm, while at 2.5 μm and 3 μm, the reflective performance exhibits varying degrees of decline.

These results show that the groove exhibits a certain degree of spatial selectivity to offsets along the *y*-axis. Variations in reflection paths and phase-matching conditions at different offsets jointly determine whether interference enhancement or suppression occurs within the structure. In particular, an offset of 2 μm appears to create more favorable conditions for coherent superposition, thereby enhancing reflective performance and significantly boosting power output.

According to the analysis of Figures 10 and 13, the groove is more sensitive to offsets along the *x*-axis, while exhibiting a certain degree of spatial selectivity along the *y*-axis under the condition of ensuring efficient coupling and reflection of the point source. Nevertheless, regardless of the light source position, the structure consistently maintains relatively good reflective performance within a certain range.

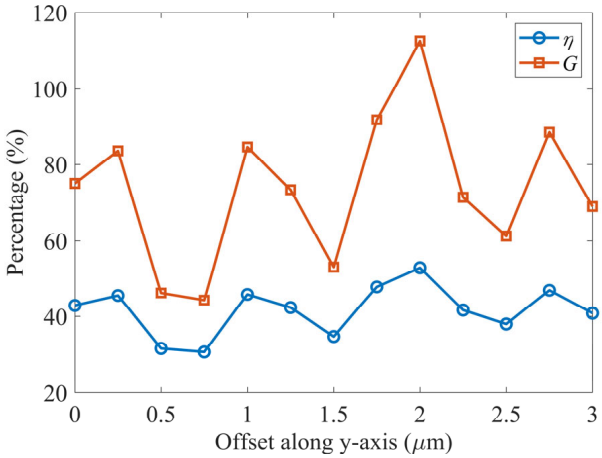

Figure 13. Effects of light source offset along the *y*-axis on reflective performance.

3.4. Analysis of the Influence of Multiple Light Sources

To examine real conditions more accurately, we further investigate the electromagnetic response of the coatings in a 10 μm-wide groove by arranging multiple point sources. Specifically, nine point sources are placed in a tilted square array, positioned at the center, the four corners, and the midpoints of the four sides of the square.

Figure 14 shows the corresponding electric field distributions. Without the coatings, the multiple point sources generate interference fringes, while about 34% of UV light is absorbed by the silicon substrate. In contrast, with the reflective coatings, we see enhanced standing wave patterns both inside and above the groove. Notably, previously downward UV light undergoes multiple internal reflections and is redirected upward.

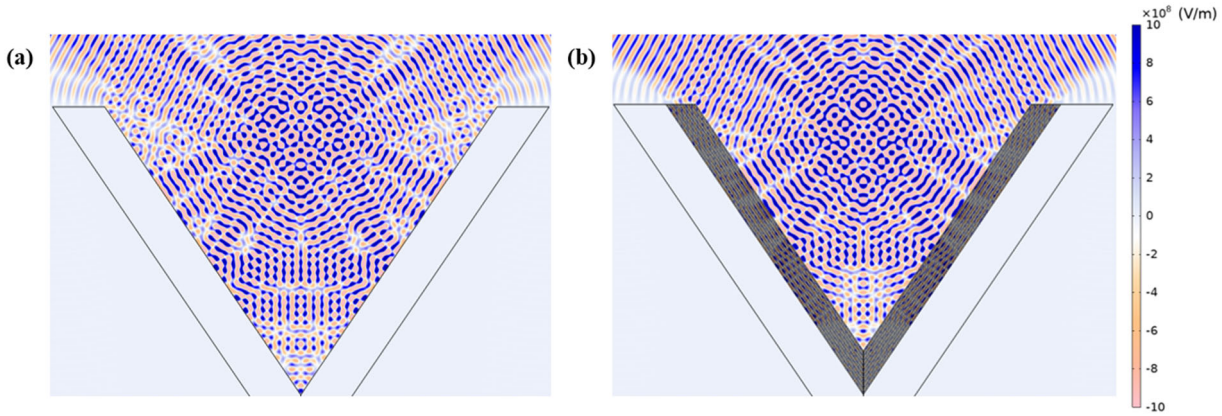

Figure 14. Electric field intensity distribution for multiple point sources. (**a**) Without the coatings. (**b**) With the reflective coatings.

The corresponding far-field radiation patterns are shown in Figure 15. Compared to the case without coatings, significantly enhanced upward radiation is found. In particular, the intensities at 45° and 135° increase by nearly threefold. This shows that the groove facilitates constructive interference within specific angular ranges, thereby enhancing upward radiation. Further calculations reveal that the reflection efficiency and power enhancement of this configuration increase to 42.35% and 73.41%, respectively. These results further confirm the effectiveness of the V-grooved reflective coatings in enhancing UV light extraction, suppressing backward losses, and improving the overall utilization efficiency of the emitted light.

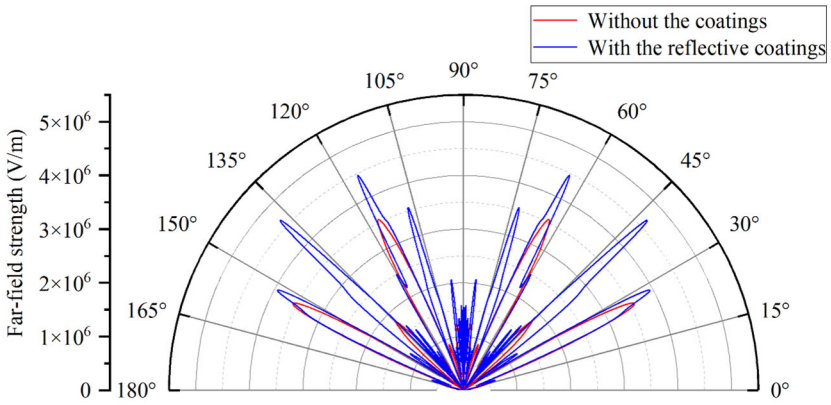

Figure 15. Far-field radiation pattern of multiple point sources.

We evaluated the reflective performance of the device under varying spacing between point sources, as shown in Figure 16. The results show that even in the lowest-performing configuration, the reflection efficiency remains close to 40%, and the power enhancement exceeds 60%. This indicates that the proposed structure exhibits stable reflective performance under different point source arrangements, effectively enhancing ultraviolet emission across a range of excitation conditions.

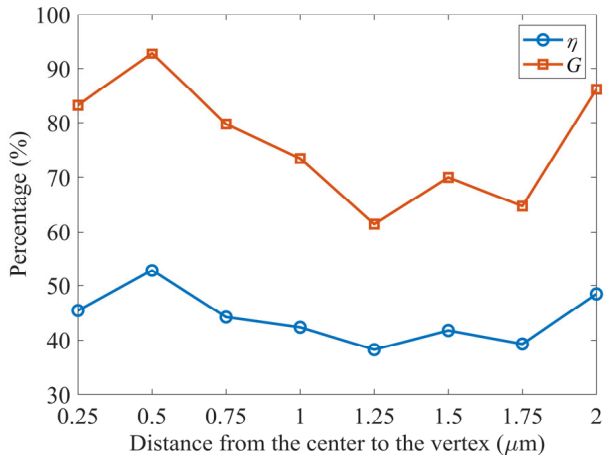

Figure 16. Effects of point source spacing on reflective performance.

We fabricate the V-shaped grooves and deposit the multilayer reflective coatings. From Figure 17, one can see that the proposed device is successfully fabricated with highly uniform and conformal coatings formed. In practical implementations, arrays containing hundreds or thousands of such grooves will be fabricated on a chip, providing cumulative UV output sufficient for applications such as disinfection and sensing. However, due to the lack of some necessary equipment, ultraviolet microplasma excitation cannot be conducted at this stage. When operated in microplasma mode, the coatings may have performance degradation due to possible heating, sputtering, transformation, and contamination.

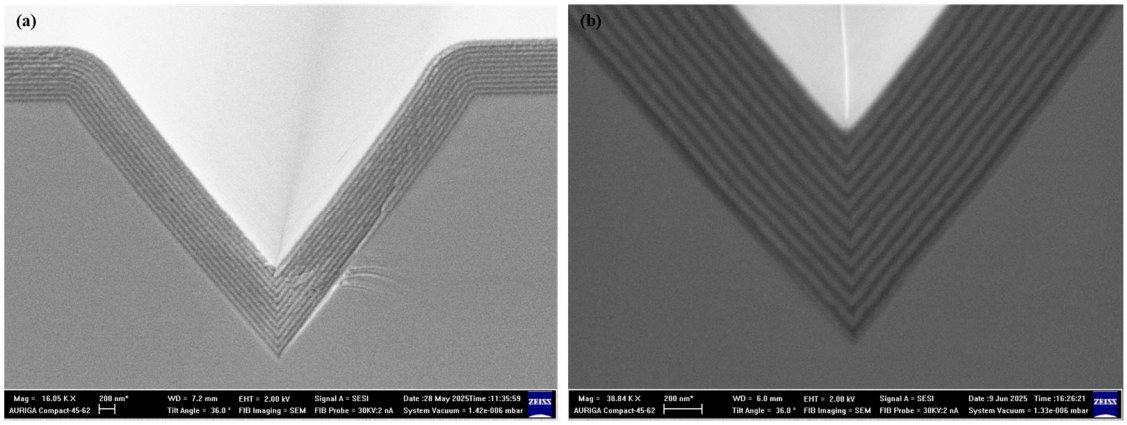

Figure 17. Deposition results of the reflective multilayer coatings. (**a**) Characterization of the V-shaped groove under scanning electron microscope. (**b**) Detailed view.

4. Conclusions

In summary, this paper presents the design of a V-shaped groove integrated with a reflective multilayer coating and demonstrates that groove width plays a critical role in determining the control capability of the optical field. At a groove width of 6.5 μm, the structure achieves optimal reflective performance, with a reflection efficiency of up to 47.82% and a power enhancement of 91.66%, corresponding to improvements of approximately 2.5-fold and 4.2-fold, respectively, compared to non-optimized groove widths. In addition, the offset of the light source significantly affects reflective performance, with offsets along the *x*-axis causing particularly large fluctuations. Therefore, in practical applications, it is essential to prioritize the precise alignment of the light source along the *x*-axis to maintain structural symmetry and consistency of reflection paths. Meanwhile, moderate adjustments of the *y*-axis position can further optimize the far-field radiation direction and enhance the control over energy, thereby achieving efficient and stable ultraviolet emission enhancement.

Author Contributions: Conceptualization, L.Z.; validation, H.Z.; formal analysis, H.Z.; investigation, H.Z. and L.Z.; resources, L.Z. and Z.H.; data curation, H.Z.; writing—original draft preparation, H.Z.; writing—review and editing, L.Z.; supervision, L.Z. and Z.H.; project administration, L.Z. All authors have read and agreed to the published version of the manuscript.

Funding: This research received no external funding.

Institutional Review Board Statement: Not applicable.

Informed Consent Statement: Not applicable.

Data Availability Statement: Data are contained within the article.

Acknowledgments: We acknowledge the support from the Advanced Integrated Optoelectronics Facility at Tianjin University.

Conflicts of Interest: The authors declare no conflicts of interest.

References

1. Lin, L.; Wang, Q. Microplasma: A new generation of technology for functional nanomaterial synthesis. *Plasma Chem. Plasma Process.* **2015**, *35*, 925–962. [CrossRef]
2. Zheng, L.; Kulkarni, P.; Diwakar, P. Spatial and temporal dynamics of a pulsed spark microplasma used for aerosol analysis. *Spectrochim. Acta Part B* **2018**, *144*, 55–62. [CrossRef]
3. Chiang, W.H.; Mariotti, D.; Sankaran, R.M.; Eden, J.G.; Ostrikov, K. Microplasmas for advanced materials and devices. *Adv. Mater.* **2020**, *32*, 1905508. [CrossRef] [PubMed]

4. Park, S.J.; Chen, J.; Wagner, C.J.; Ostrom, N.P.; Liu, C.; Eden, J.G. Microdischarge arrays: A new family of photonic devices. *IEEE J. Sel. Top. Quantum Electron.* **2002**, *8*, 387–394. [CrossRef]
5. Becker, K.H.; Schoenbach, K.H.; Eden, J.G. Microplasmas and applications. *J. Phys. D Appl. Phys.* **2006**, *39*, R55. [CrossRef]
6. Schoenbach, K.H.; Becker, K. 20 years of microplasma research: A status report. *Eur. Phys. J. D* **2016**, *70*, 29. [CrossRef]
7. Nijdam, S.; Desai, K.V.; Park, S.J.; Sun, P.P.; Sakai, O.; Lister, G.; Eden, J.G. Foundations of plasma photonics: Lamps, lasers, and electromagnetic devices. *Plasma Sources Sci. Technol.* **2023**, *31*, 123001. [CrossRef]
8. Thaury, C.; Quere, F.; Geindre, J.P.; Levy, A.; Ceccotti, T.; Monot, P.; Bougeard, M.; Réau, F.; d'Oliveira, P.; Audebert, P.; et al. Plasma mirrors for ultrahigh-intensity optics. *Nat. Phys.* **2007**, *3*, 424–429. [CrossRef]
9. Leblanc, A.; Denoeud, A.; Chopineau, L.; Mennerat, G.; Martin, P.; Quéré, F. Plasma holograms for ultrahigh-intensity optics. *Nat. Phys.* **2017**, *13*, 440–443. [CrossRef]
10. Kunze, K.; Miclea, M.; Franzke, J.; Niemax, K. The dielectric barrier discharge as a detector for gas chromatography. *Spectrochim. Acta Part B* **2003**, *58*, 1435–1443. [CrossRef]
11. Stoffels, E.; Flikweert, A.J.; Stoffels, W.W.; Kroesen, G. Plasma needle: A non-destructive atmospheric plasma source for fine surface treatment of (bio) materials. *Plasma Sources Sci. Technol.* **2002**, *11*, 383. [CrossRef]
12. Laroussi, M.; Lu, X.P. Room-temperature atmospheric pressure plasma plume for biomedical applications. *Appl. Phys. Lett.* **2005**, *87*, 113902. [CrossRef]
13. Shirai, H.; Kobayashi, T.; Hasegawa, Y. Synthesis of silicon nanocones using rf microplasma at atmospheric pressure. *Appl. Phys. Lett.* **2005**, *87*, 143112. [CrossRef]
14. Anderson, M. The ultraviolet offense: Germicidal UV lamps destroy vicious viruses. New tech might put them many more places without harming humans. *IEEE Spectr.* **2020**, *57*, 50–55. [CrossRef]
15. Ma, B.; Bright, K.; Ikner, L.; Ley, C.; Seyedi, S.; Gerba, C.P.; Sobsey, M.D.; Piper, P.; Linden, K.G. UV inactivation of common pathogens and surrogates under 222 nm irradiation from KrCl* excimer lamps. *Photochem. Photobiol.* **2023**, *99*, 975–982. [CrossRef] [PubMed]
16. García de Abajo, F.J.; Hernández, R.J.; Kaminer, I.; Meyerhans, A.; Rosell-Llompart, J.; Sanchez-Elsner, T. Back to normal: An old physics route to reduce SARS-CoV-2 transmission in indoor spaces. *ACS Nano* **2020**, *14*, 7704–7713. [CrossRef]
17. Frame, J.W.; Wheeler, D.J.; DeTemple, T.A.; Eden, J.G. Microdischarge devices fabricated in silicon. *Appl. Phys. Lett.* **1997**, *71*, 1165–1167. [CrossRef]
18. Park, S.J.; Chen, J.; Liu, C.; Eden, J.G. Arrays of microdischarge devices having 50–100 μm square pyramidal Si anodes and screen cathodes. *Electron. Lett.* **2001**, *37*, 171–172. [CrossRef]
19. Eden, J.G.; Park, S.J. Microcavity plasma devices and arrays: A new realm of plasma physics and photonic applications. *Plasma Phys. Control. Fusion* **2005**, *47*, B83–B92. [CrossRef]
20. Wu, C.; Hoskinson, A.R.; Hopwood, J. Stable linear plasma arrays at atmospheric pressure. *Plasma Sources Sci. Technol.* **2011**, *20*, 045022. [CrossRef]
21. Eden, J.G.; Park, S.J.; Herring, C.M.; Bulson, J.M. Microplasma light tiles: Thin sheet lamps for general illumination. *J. Phys. D Appl. Phys.* **2011**, *44*, 224011. [CrossRef]
22. Wang, Y.; Ni, J.H.; Zhong, S.; Zhang, X.; Liang, Z.; Liu, C.; Park, S.J.; Eden, J.G. Microplasma mode transition and corresponding propagation characteristics controlled by manipulating electric field strength in a microchannel-cavity hybrid structure device. *J. Phys. D Appl. Phys.* **2016**, *49*, 415206. [CrossRef]
23. Park, S.J.; Herring, C.M.; Mironov, A.E.; Cho, J.H.; Eden, J.G. 25 W of average power at 172 nm in the vacuum ultraviolet from flat, efficient lamps driven by interlaced arrays of microcavity plasmas. *APL Photonics* **2017**, *2*, 041302. [CrossRef]
24. Dzikowski, S.; Michaud, R.; Böttner, H.; Dussart, R.; Böke, M.; Schulz-von Der Gathen, V. Modular constructed metal-grid arrays—An alternative to silicon-based microplasma devices for catalytic applications. *Plasma Sources Sci. Technol.* **2020**, *29*, 035028. [CrossRef]
25. Sun, J.; Li, X.; Zhang, W.; Yi, K.; Shao, J. High-reflectivity mirrors by Al_2O_3, LaF_3 and AlF_3 for 193 nm application. *Opt. Laser Technol.* **2014**, *56*, 65–70. [CrossRef]
26. Narukage, N.; Kubo, M.; Ishikawa, R.; Ishikawa, S.N.; Katsukawa, Y.; Kobiki, T.; Giono, G.; Kano, R.; Bando, T.; Tsuneta, S.; et al. High-reflectivity coatings for a vacuum ultraviolet spectropolarimeter. *Sol. Phys.* **2017**, *292*, 40. [CrossRef]
27. Kim, J.; Mironov, A.; Park, S.; Kim, C.; Park, S.J.; Eden, J.G. Ultrasound harmonic generation and atomic layer deposition of multilayer, deep-UV mirrors and filters with microcavity plasma arrays. *Eur. Phys. J. D* **2023**, *77*, 73. [CrossRef]
28. Jia, X.; Kapraun, J.; Wang, J.; Qi, J.; Ji, Y.; Chang-Hasnain, C. Metasurface reflector enables room-temperature circularly polarized emission from VCSEL. *OPTICA* **2023**, *10*, 1093–1099. [CrossRef]
29. Yuan, L.; Fan, S. Temporal modulation brings metamaterials into new era. *Light Sci. Appl.* **2022**, *11*, 173. [CrossRef]
30. Oton, E.; Cigl, M.; Morawiak, P.; Mironov, S.; Bubnov, A.; Piecek, W. All-optical 3D blue phase photonic crystal switch with photosensitive dopants. *Sci. Rep.* **2024**, *14*, 9910. [CrossRef]
31. Yu, D.; Tan, H. *Engineering Optics*, 4th ed.; China Machine Press: Beijing, China, 2015; pp. 376–380. ISBN 978-7-111-51962-1.

32. Boidin, R.; Halenkovič, T.; Nazabal, V.; Beneš, L.; Němec, P. Pulsed laser deposited alumina thin films. *Ceram. Int.* **2016**, *42*, 1177–1182. [CrossRef]
33. Rodríguez-de Marcos, L.V.; Larruquert, J.I.; Méndez, J.A.; Aznárez, J.A. Self-consistent optical constants of SiO_2 and Ta_2O_5 films. *Opt. Mater. Express* **2016**, *6*, 3622–3637. [CrossRef]
34. Berenger, J.P. A perfectly matched layer for the absorption of electromagnetic waves. *J. Comput. Phys.* **1994**, *114*, 185–200. [CrossRef]
35. Xie, S.; Pedrow, P.D. A novel active needle probe in an atmospheric pressure corona-based cold plasma reactor with admixtures of helium and dry air. *IEEE Trans. Plasma Sci.* **2020**, *48*, 2418–2430. [CrossRef]